Editors' Suggestion

Power in numbers: Emergent thermodynamic and kinetic cooperativity from biomolecular condensate growth

Caleb Huang and B. Montgomery Pettitt*
Biochemistry and Molecular Biology, University of Texas Medical Branch, Galveston, Texas 77555-0304, USA

(Received 17 October 2025; revised 12 May 2026; accepted 26 May 2026; published 17 June 2026)

Biomolecular condensates provide a platform to modulate intracellular chemical reaction efficiency, yet how condensate size and sequence dependence are related to solubility and relaxation kinetics remains unsettled. All-atom simulations of model glycine-rich pentapeptides spanning nearly 2 orders of magnitude in aggregate size were used to connect observations of microscopic interactions among intrinsically disordered proteins and water to mesoscopic laws of condensed matter physics. The models used here show that growth induces two forms of cooperativity. Thermodynamic cooperativity lowers apparent solubility with increasing radius, which is consistent with the Ostwald-Freundlich equation. The characteristic radius in the equation marks a significant reduction in the change in solubility with increased radius. This coincides with the formation of a dense inner core of peptides that traps a subpopulation of waters. Kinetic cooperativity slows peptide exchange with increasing radius. The peptide turnover rate for the condensate in terms of survival probability was characterized. The peptide survival curves for different sized condensates and sequences follow a bifurcated Kohlrausch-Williams-Watts stretched-exponential model, which is consistent with short-range van der Waals forces dominating peptide retention at the condensate-water interface, while long-range electrostatic forces dominate peptide properties deeper within the core. Our model condensates exhibit viscoelastic properties different from Newtonian fluids like water. Our findings underscore the need to incorporate cooperative effects into biophysical models for condensates.

DOI: 10.1103/kbfb-d5nk

I. INTRODUCTION

Molecular self-assembly is a hallmark of biological organization, encompassing protein folding, supramolecular oligomerization, and the formation of biomolecular condensates—liquidlike structures enriched with intrinsically disordered proteins, which lack a fixed structure of their own [1]. These assemblies have been reported to span from nanometer to micrometer in size and are highly dynamic in nature [2–5]. Yet, how condensate size feeds back on thermodynamic stability and relaxation kinetics is not well understood.

Classical nucleation expectations and Lifshitz-Slyozov-Wagner theory of coarsening posit a critical radius for growth [6] and predict Ostwald ripening [7] in condensates, wherein larger droplets subsist at the expense of smaller ones. Ostwald ripening predicts that only one condensate remains

*Contact author: mpettitt@utmb.edu

at thermodynamic equilibrium. The persistence of multitudes of intracellular condensates varying in sizes indicates that biological systems regulate condensate stability far from equilibrium [5].

The biological consequences of condensate size variation, even comparing across condensates composed of the same proteins, are evident in various physiological and pathological contexts. In the mitogen-activated protein kinase known as (MAPK) signaling pathway, receptor tyrosine kinase aggregates influence cell outcomes, with large, short-lived clusters promoting proliferation and small, long-lived clusters favoring differentiation [8–10]. At DNA repair sites, Ostwald ripening of condensates composed of tumor suppressor p53 is suppressed by MDM2 to keep condensates at an optimal radius and prevent the formation of a single large condensate [11]. In cancer, the nucleoli size is associated with reduced cell-doubling time and worsened prognosis [12,13]. In neurodegenerative diseases, the formation of oligomers, which consist of small assemblies of amyloid-β [14] or tau [15,16], has been identified as a potential precursor to larger liquid condensates, which then finally rearrange into solid plaques, a feature pathognomonic for the disease, though the type of aggregate that contributes to neuron death is still debated [17]. This is not unlike the metastable liquid droplets that proceed crystal growth from solution near solid steps and defects [18].

Despite growing evidence that condensate size modulates function, there remain fundamental questions about the thermodynamic and kinetic properties of condensates. Thermodynamically, the minimum size at which an aggregate is no longer considered a precondensate (also sometimes described as a "dynamic hub" or "oligomeric complex") but a condensate is ill-defined and remains an open issue [19]. Kinetically, the monomer dissociation rate constant (k_{off}) is often assumed to be independent of condensate size and location within the condensate, and the survival function is thus typically assumed to be a simple exponential Markovian process [20]. However, exponential measurements can be imprecise by orders of magnitude, suggesting that the first-order kinetic model for dissociation rates, which assumes independence, may not be sufficient [20–22]. Indeed, molecular assembly rates have been derived analytically to have fractal-like kinetics [23]. Recently, Mittag and Pappu have suggested revising some of the assumptions in the term "liquid-liquid phase separation" as many condensates exhibit viscoelastic properties different from a simple Newtonian fluid [24].

To address these questions, an all-atom computational simulation model consisting of concentrated solutions of pentapeptide motifs (GGXGG, X = S, G, Y) is employed across a range of different aggregate sizes, with both peptide solubility and aggregate size spanning over an order of magnitude. The glycine-rich GGXGG peptide motif has been extensively used to study aggregates as it models the flexibility of intrinsically disordered proteins but is simple enough to derive theoretical conclusions [25–29]. The simulations done here are to mimic the intracellular behavior of small condensate formations limited by material within a volume [3,4]. Since a cell is not at equilibrium globally, we have mimicked the local concentrations leading to droplets within crowded, compartmentalized cells by considering a series of smaller volumes that are oversaturated.

This work quantifies peptide and water structure and dynamics as functions of radius, leading to a unified picture in which growth generates two forms of cooperativity: a thermodynamic cooperativity—a curvature-controlled decrease of apparent solubility with radius—and a kinetic cooperativity—a systematic slowing of exchange accompanied by stretched-exponential survival. A characteristic radius is found, beyond which a core-shell density architecture emerges, thus arguing for a need to distinguish more precisely between *precondensates* and *condensates*. Overall, the model biomolecular condensates display emergent, cooperative-network behavior, like described in drone swarms [30] or human society [31], arising from an ensemble of microscopic interactions leading to mesoscale phenomena that cannot be predicted by a sum of individual pairwise reactions, e.g., $\mathrm{A} + \mathrm{A} \rightarrow 2\mathrm{A}$.

II. RESULTS

The simulations modeled the behavior of peptide aggregate structure and dynamics in aqueous environments as a function of aggregate size. Here, *aggregate* is defined as a general term that

encompasses peptide assemblies of any size and does not discriminate between *precondensate* and *condensate*, to be differentiated below. The details of the calculations are given in Sec. V. Briefly, 21 simulations (7 system sizes × 3 peptide sequence motifs) with molecular dynamics and a conventional all-atom, nonpolarizable force field were performed [32]. All used a nonequilibrium supersaturated initial condition of 0.3 M in a cubic volume at constant pressure and temperature (NPT) and all had 80%–99% of the peptides rapidly coalesce into a single approximately spherical aggregate. This result reflects the limited growth of the aggregate by the available peptides in the simulation volume. In our simulations, each different resulting condensate reflects a possible state in the nonequilibrium growth of a larger aggregate. The relation between the median aggregate radius and the number of peptides in the condensate fitted a cube root relationship, as expected. The condensates exhibit significant surface roughness, as shown by the range between the minimum and maximum radii of the condensate boundaries (Fig. 1). The minimum dimension corresponds to the radius of the inner core, and the maximum dimension corresponds to the radius extending to the edge of outer shell, together which defines a core-shell architecture (Fig. 2) as seen in other recent peptide condensate work [33].

A. Condensate size lowers apparent solubility

The apparent solubility, i.e., the directly measured solubility, is found to be related to the aggregate radius by the exponential of the reciprocal function [Fig. 1(b) and Fig. S2(A) of the Supplemental Material [34]]. This is consistent with a form of the Ostwald-Freundlich equation and the Gibbs-Thomson curvature effect [35,36], which describes increasing stability of droplet with growth:

$$c(r) = c_\infty \exp\left(\frac{2\gamma v}{\phi k_B T r}\right), \tag{1}$$

where $c(r)$ is the apparent solubility, c_∞ is the solubility at the macroscopic limit, γ is the interfacial tension, v is the peptide molecular volume, ϕ is the peptide volume fraction in the aggregate, r is the radius of the aggregate, k is the Boltzmann constant, and T is the temperature.

The common form ($\phi = 1$) is based on the approximation that the condensate is pure or has little solvent [35]. A more general form exists, as shown by Pérez, which modifies the exponential with the concentration of the pure condensate [35]. The water density is explicitly calculated in the condensate as a function of sequence, distance from the condensate center, and radius in Sec. II B. Given that the condensate is ∼25% water by volume, it can be inferred that the condensate is 75% peptide by volume, i.e., $\phi = 0.25$. Calculation of surface tension γ reveals 11–13 mN/m for all peptide motifs [Fig. S2(A) of the Supplemental Material [34]]. This is 1 order of magnitude lower than oil in water (50 mN/m) [37] and 1–3 orders of magnitude higher than coacervates, like FUS, Whi3, and LAF1 (0.005–0.5 mN/m) [38,39].

The solubility limits for S, G, and Y extrapolated at the planar limit were determined to be 22.9, 10.4, and 0.17 mM, respectively, roughly two-thirds of the solubility for the 625-X systems. Notably, the observed trend for the model force field used aligned with known experimental solubility limits for serine, glycine, and tyrosine (S > G > Y) amino acids [40].

A characteristic radius, defined as r^* when $c(r^*) = e^1 c_\infty \approx 2.7 c_\infty$ (which solves to $r^* = 2\gamma v/\phi kT$), is the point above which the change in solubility dramatically decreases with increasing size [Fig. S2(A)]. The characteristic or lower-bound radius for all pentapeptide motifs studied here is near 2 nm, with a corresponding inner core radius of 1.5 nm [Fig. 1(b)]. This works out to an aggregate size of approximately 50 peptides, corresponding to the 78-S, 78-G, and 39-Y systems. As discussed below, the inner core structure results from explicit peptide-water correlations both spatially and dynamically.

For clarity, aggregates below the characteristic radius are labeled as *precondensates* and aggregates above the characteristic radius as *condensates*. This scheme is justified by showing that *precondensates* and *condensates*, using the characteristic radius definition, have consistently

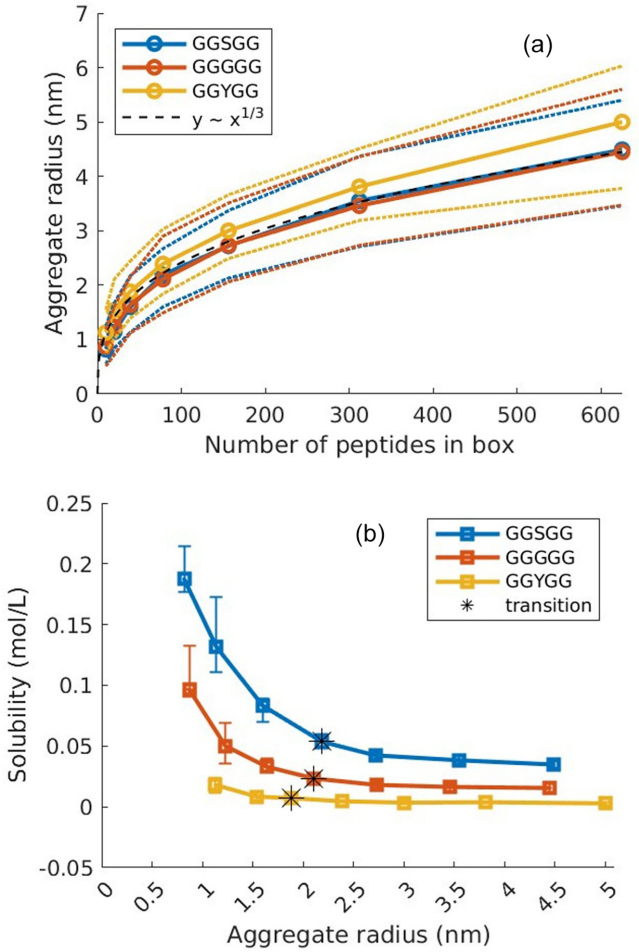

FIG. 1. Thermodynamic cooperativity: Solubility obeys curvature-controlled scaling and reveals a 2-nm characteristic radius. (a) Median radius of aggregate (solid line) and minimum (10th percentile) and maximum (90th percentile) radii (dotted lines). The function $y \propto x^{1/3}$ (black dashed line) shows that the median aggregate radius followed the cube root of system size well. (b) Solubility limit is dependent on radius for small aggregate sizes but levels off asymptotically. Data fit the Ostwald-Freundlich equation $c(r) = c_\infty e^{2\gamma v/\phi rkT}$ [extended data in Fig. 2(a)]. The characteristic radius r^* for the equation, i.e., $c(r^*) = e^1 c_\infty = 2.7c_\infty$, is in the neighborhood of $r^* = 2$ nm for all three peptide motifs. Error bars represent 95% confidence intervals estimated by bootstrap resampling (2.5th–97.5th percentiles).

qualitatively different structural and dynamical properties, thus illustrating its potential biophysical significance.

B. Characteristic radius coincides with distinct condensate core-shell formation with subpopulation of bound waters

As the roughly 2 nm characteristic radius lies between the 39-S and 78-S systems, focus is given to the 39-S system as the largest precondensate, the 78-S system as the smallest condensate, and the 625-S system as a reference condensate well beyond the characteristic radius. Water and peptide radial density distribution functions, $\rho(r)$ [41], from the aggregate center of geometry were calculated [Fig. 2(a) and Figs. S1(G)–S1(I) of the Supplemental Material [34]]. The last significant

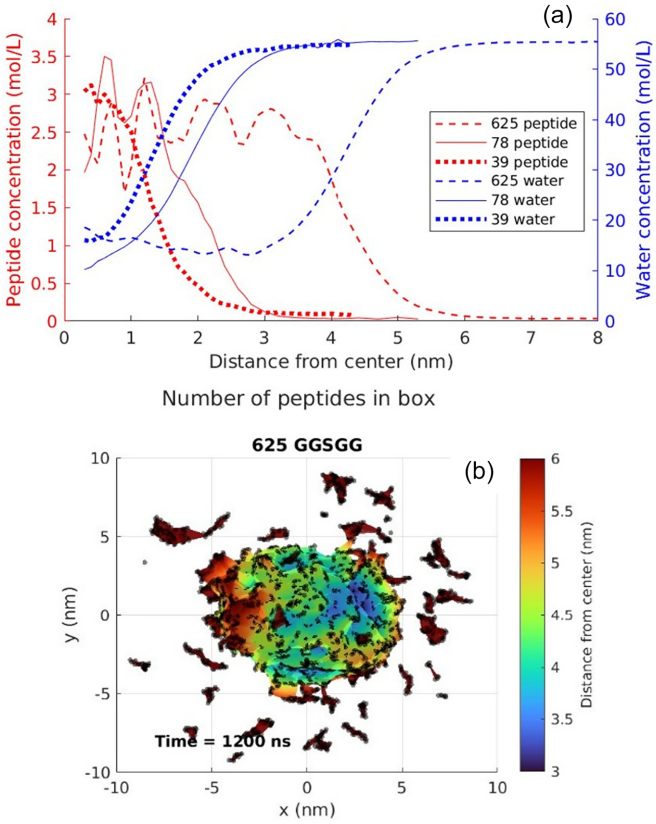

FIG. 2. Layered inner core-outer shell architecture emerges at the 2-nm characteristic radius. (a) Water and GGSGG peptide density relative to aggregate center for 39-S, 78-S, and 625-S systems. Corresponding to the characteristic radius (2 nm), the 78-S system is required for two peptide layers in the inner core (1.5 nm). (b) The 625-S peptide system shows a condensate with an inner core that extends to 4 nm, well beyond the minimum ∼1.5 nm inner core defining a precondensate from a condensate, and an outer shell that extends to 5 nm. Color bar indicates peptide distance from condensate center of geometry, visualized as a three-dimensional projection of peptides onto an x–y plane. Approximately 50 peptides are soluble and diffuse freely in solution. See Video S1 of the Supplemental Material [34] for dynamics.

peak, based on our configurational sampling, corresponded with the minimum aggregate dimension, i.e., the inner core [Figs. 2(a) and 2(b)]. For the 625-S system, there were approximately five $\rho(r)$ peaks, initially spaced 0.7–0.8 nm apart, consistent with just under twice the radius of gyration of the pentaglycine (∼0.4 nm) [42]. The condensate, which had a median radius of 4.5 nm, formed a spherical inner core with a radius that corresponded to the ∼4 nm (10th percentile) and dynamic liquidlike protrusions reminiscent of capillary waves that extended to ∼5 nm (90th percentile) [Fig. 2(b) and Video S1 of the Supplemental Material [34]]. The numbers of identifiable peaks were 2 and 1 for the 78-S (condensate) and 39-S (precondensate) systems, respectively. For all three peptide types, the presence of two peptide layers at the inner core marks the transition from precondensate to condensate [Fig. S1(B) of the Supplemental Material [34]].

Regardless of aggregate radius or peptide type, the peptide and water densities converged to approximately 3 and 15 M, respectively [see Fig. 2(a) and Fig. S1(B) of the Supplemental Material [34] for all system sizes and peptide types]. This corresponded to approximately five water molecules per peptide or one water molecule per amino acid residue in the inner core. Given a bulk water concentration of 55 M, the condensate is 25% water, which lies somewhere between

an effectively dry interior of solidlike amyloid fibrils [43] and 73% water by volume in complex coacervates composed of the Dead box RNA helicase (DDx4) [44] with many other systems in the intermediate range [45].

While water converged to 15 M for both precondensates and condensates, each exhibited significant differences in water dynamics. A subpopulation of bound water with residence times (duration that a water molecule stays near an arbitrary reference point) greater than 15 ns was found in the inner core, illustrated in the 78-S or 625-S system (Fig. 3). Note that the bound waters have roughly 100–1000 times the residency of either water near an aqueous or condensate surface peptide. In the precondensate, where there are fewer than two complete layers of peptides in the inner core, the water behavior is more nearly bulklike [Fig. 3(a)]. Analysis of all peptide motifs shows that a minimum of two complete peptide layers at the inner core were required for bound waters [Figs. S1(G)–S1(I) and S3 of the Supplemental Material [34]].

C. Exchange slows with size and follows stretched-exponential survival

The kinetic stability of peptides in aggregate, measured by half-life (time to reduce to half of the initial value), exhibited a positive correlation with size (Fig. 4), following $t_{1/2} \propto r^{2.5}$ with the exponent ranging from 2.3 to 3.4 [Fig. S2(B) of the Supplemental Material [34]]. The 5-nm 625-Y system, based on the extrapolated relation, is estimated to have a half-life of 10 μs, longer than is computationally convenient for reasonable statistics. While overall the kinetic stability ranked as Y > G > S, when comparing across the same system sizes, the ranking changed across different sizes. The 625-S system (4.5 nm), for instance, was kinetically more stable than the 156-G (2.75 nm), which was in turn more stable than 39-Y (2 nm) (500 ns versus 400 ns versus 300 ns, respectively).

The lifetime of aggregate peptides was investigated as a function of survival curve. For the 625-S system, each radial layer of the aggregate exhibited a very different survival curve and thus unbinding rate, k_{off} [Fig. 4(b)]. This arises from differential trapping experienced by peptides in different layers, resulting in an overall survival curve with a stretched exponential decay pattern [Fig. 4(b) for the 625-S system and Fig. S6 of the Supplemental Material [34] for all 21 systems]. Phillips derived a survival curve argument for a bifurcated stretched exponential, β, $S(t) = e^{-(t/\tau)^{\beta}}$, where $\beta = 3/5$ for short-range van der Waals forces and $\beta = 3/7$ for long-range Coulombic forces that can be applied to the structural relaxation of viscous polymers [46]. The early time interval of survival curves of all aggregates (200, 400, and 500 ns for serine, glycine, and tyrosine, respectively), which primarily corresponded to exchange of the outer shell, was fitted to the stretched exponential function with β and τ as parameters. $\beta = 3/5$ was found independent of aggregate size or peptide chemical identity [Figs. 4(a) and 4(b) and Fig. S4 of the Supplemental Material [34]].

Note that $\beta = 3/5$ is an excellent fit for the outer shell, which is effectively the entire survival curve of the precondensate 39-X systems. However, for condensates, $\beta = 3/7$ is a better fit after most of the outer shell has been exchanged, suggesting that the ripened inner core, characterized by bound waters, is dominated by electrostatic forces [Figs. 4(a) and 4(b) and Fig. S4 of the Supplemental Material [34]]. To determine the generalizability of this finding, an ionic system of supersaturated 2.6 M Na_2HPO_4 salt (containing 625 molecules) whose force field parameters had been optimized to fit experimental solubility previously was considered [47]. Here, the aggregate fit $\beta = 3/5$ for the first 100 ns and bifurcated to $\beta = 3/7$ from 200 to 500 ns (Fig. S7 of the Supplemental Material [34]).

Water molecules in an aggregate exhibited different kinetic behaviors compared to peptides in aggregate [Figs. 4(c) and 4(d)]. The waters in precondensates were effectively near bulk water with a half-life of less than 1 ns, while subpopulations of waters in the condensates were moderately bound, with a half-life of 10–30 ns [Fig. 4(c)]. While the kinetics of bound water in condensate was independent of size, they did depend on peptide identity, ranking as Y (∼25 ns) > G ≈ S (∼15 ns), indicating that water's interactions with specific chemical moieties like aromatic rings are more important than the physical distance required to travel out of the aggregate.

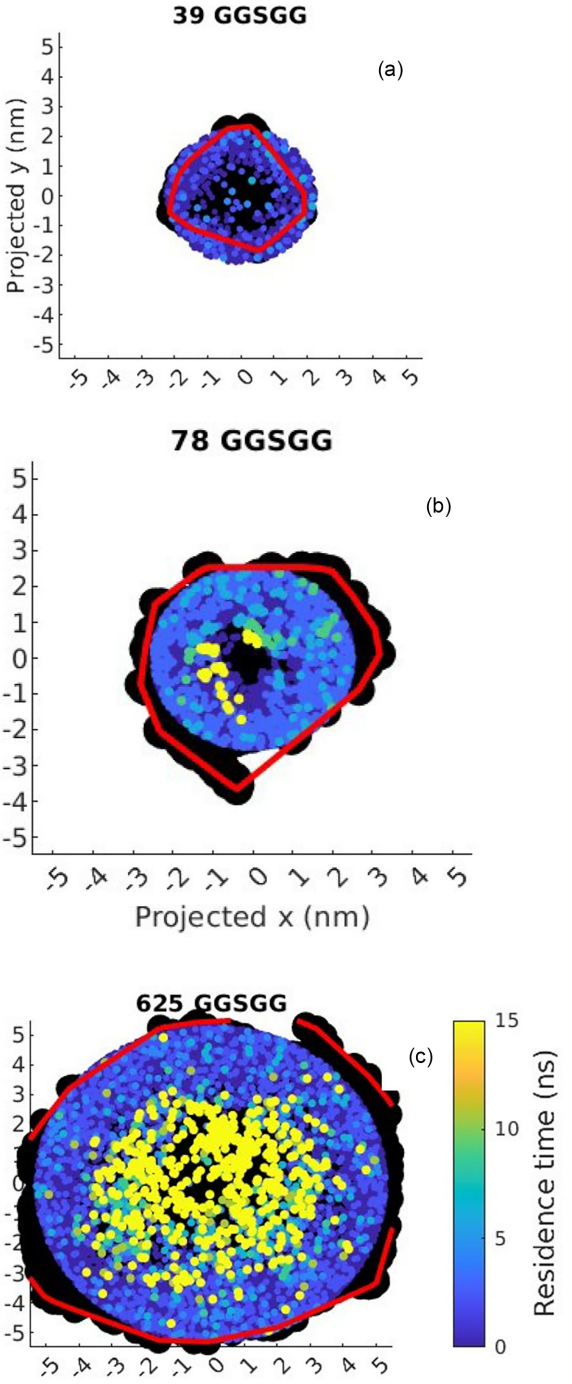

FIG. 3. Bound-water subpopulation appears only beyond the characteristic radius and localizes to the inner core. Radial distribution of the lifetime of water (colored) against peptides (black) for (a) 39-S system, (b) 78-S system, and (c) 625-S system as an ensemble over 15 ns. The outline (red) shows the convex hull around a single aggregate in time. The data show that an inner core radius of 1.5 nm is the minimum radius to hold bound water.

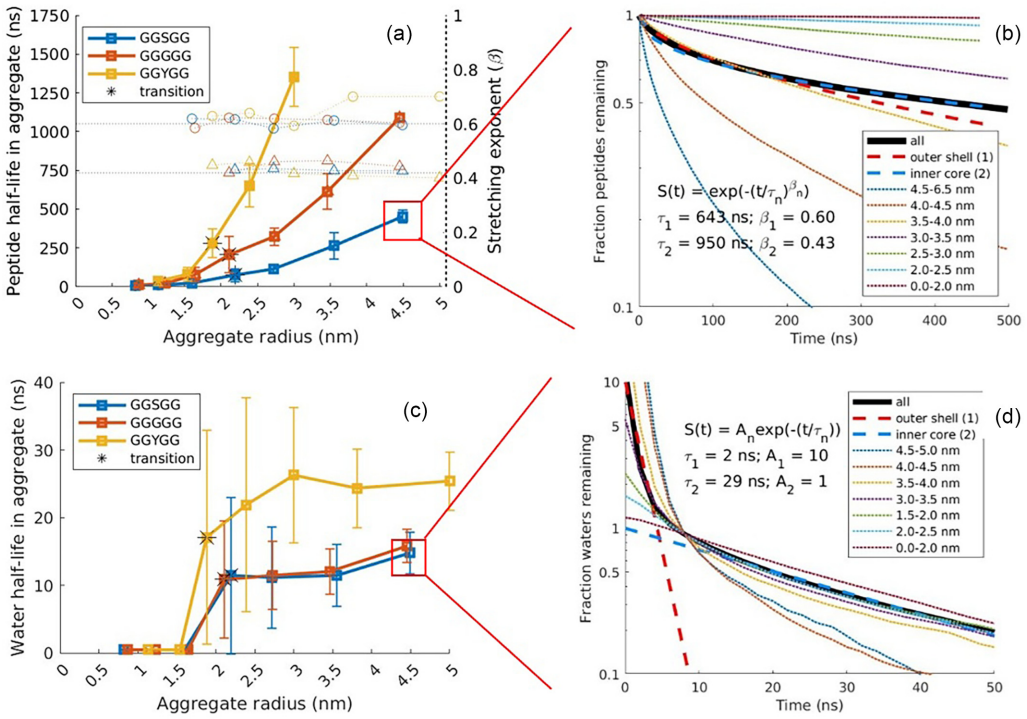

FIG. 4. Kinetic cooperativity: Increasing radius slows exchange and yields bifurcated stretched-exponential survival for peptides, unlike water. (a) The peptide half-life of a condensate is dependent on size and amino acid (S vs G vs Y). The two stretching exponents β for each survival curve (example shown in inset) are reported, with the initial time interval corresponding to outer shell exchange marked with an open circle and the latter time interval corresponding to the inner core marked with an open triangle. Reference values $\beta = 3/5$ and 3/7 marked in the black dashed line. See extended data in panel (b) for curve fit for all peptides. (b) The 625-S system shows a transition from rapid outer shell exchange to stable inner core exchange at 150 ns. Stretched exponent fitting shown in extended data in panel (a). (c) Water half-life in condensate is dependent on amino acid type (tyrosine vs glycine and serine) but independent of condensate size beyond 78 peptides. (d) The half-life of water is obtained from the survival curve, which consists of a rapidly decaying unbound population and a slowly decaying bound population. The water lifetime is independent of distance from condensate center of geometry.

The water survival curve in condensate was well fit with a biexponential curve, showing two populations of water: a fast, bulklike component and a slow, bound component [Fig. 4(d) for 625-S; see Fig. S10 of the Supplemental Material [34] for all aggregates]. A change in slope was observed at approximately 10 ns, marking a transition from fast to slow behavior. The fast, bulklike waters had a survival time 1 order of magnitude faster than bound waters, which in turn have a survival time 1–2 orders of magnitude lower than peptides (10^0 ns versus 10^1 ns versus 10^2–10^3 ns, respectively). Each radial layer of water exhibited a similar bound water survival curve and thus unbinding rate k_{off}.

D. Condensate diffusion follows exponential decay in peptides and binary drop in water

Consistent with the variable survival rates across different aggregate sizes and relative location within an aggregate, the diffusion coefficient decayed exponentially from the surface of the aggregate [Figs. 5(a) and 5(c)]. Being interested in large (order-of-magnitude) changes in diffusion

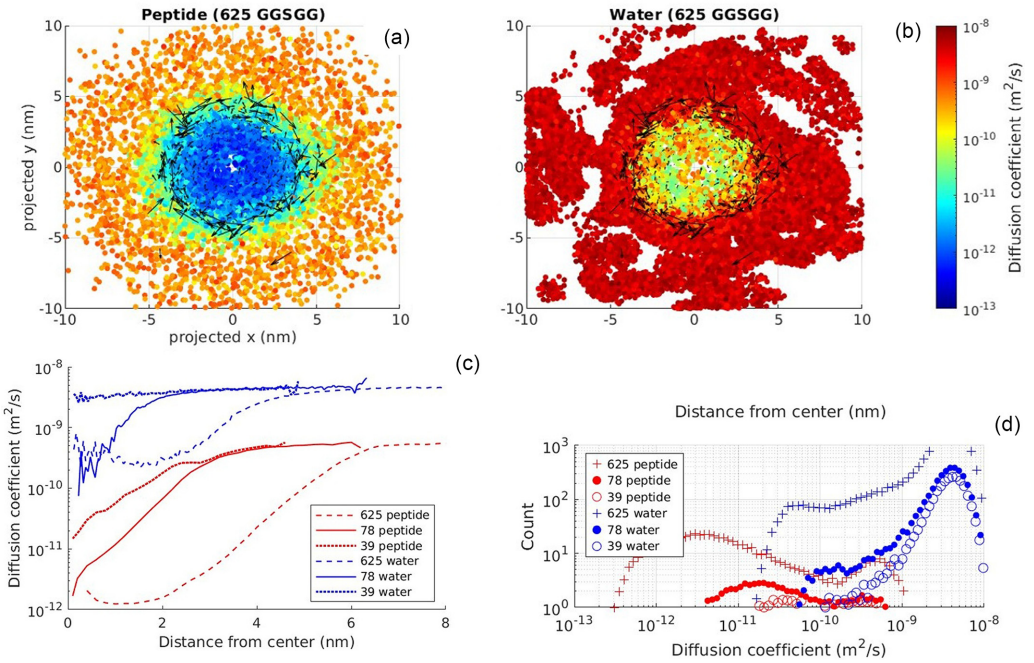

FIG. 5. Peptides experience anisotropy at the outer shell and exponential slowing toward the core, while water transitions from bulk to bound in a switchlike, two-state manner. Projected spatial map of the 625-S system showing (a) diffusion coefficients of peptides (ensemble) and (b) diffusion coefficients of waters within 0.6 nm of peptides (single snapshot). Colors are scaled equally for both plots. Overlaid on both plots is a quiver plot showing the displacement of peptides after 20 ns (vector magnitude corresponds to axis scale; threshold at 2 nm). All calculations are corrected for net droplet translational and rotational motion. The position of all data points corresponds to their reference position. (c) Diffusion coefficient vs distance from center for peptides and waters for the 625-S, 78-S, and 39-S systems. Peptides exhibit exponential dependence on radius with respect to center of geometry, while waters have a sharper transition from bulk to bound as they enter the inner core of the condensate, also seen in panel (b). (d) Distribution of peptide and water diffusion coefficients for 625-S, 78-S, and 39-S systems.

coefficients, a linear relation between mean squared displacement and time corresponding to classical Brownian motion was assumed (details given in Sec. V). However, previously it was shown that the center of the condensate core interior experienced constrained, anomalous diffusion with a subdiffusive exponent of 0.5 [48]. The rate of decay as a function of distance from the surface was roughly constant between condensate sizes. The diffusion coefficient dropped 2–3 orders of magnitude from $\sim 5 \times 10^{-10}\,\mathrm{m}^2/\mathrm{s}$ for peptides in aqueous solution to $\sim 1 \times 10^{-12}\,\mathrm{m}^2/\mathrm{s}$ for peptides at the inner core.

The outer shell held a dynamic population of peptides at $\sim 5 \times 10^{-11}\,\mathrm{m}^2/\mathrm{s}$ whose displacements were highly anisotropic and primarily parallel to the surface [Fig. 5(a) and Video S2 and Fig. S5 of the Supplemental Material [34]], even after correcting for net rotation of the condensate, indicating a higher energy barrier for peptides to move perpendicular to the surface of the condensate. Condensates above the characteristic radius (78-S and 625-S) converge to $1 \times 10^{-12}\,\mathrm{m}^2/\mathrm{s}$ at the inner core, while the 39-S precondensate converges to 1×10^{-11} [Fig. 5(c)].

Water also experienced a 2 order-of-magnitude drop in diffusion coefficient from $\sim 5 \times 10^{-9}\,\mathrm{m}^2/\mathrm{s}$ in solution to $\sim 5 \times 10^{-11}\,\mathrm{m}^2/\mathrm{s}$ for a subpopulation of bound waters in all condensates [Figs. 5(b)–5(d) and Figs. S5 and S6 of the Supplemental Material [34]]. Several key differences exist between diffusion of peptide and water, however. Water diffusion in the outer shell of the

condensate was effectively the same as bulk water. It dropped precipitously at the inner core of the condensate, though with a large variability, with subpopulations of bound (5×10^{-11} m^2/s) and bulklike water (5×10^{-9} m^2/s). For precondensates, the water diffusion was dampened relative to bulk water but did not reach an asymptote level lower than 1×10^{-10} m^2/s [Figs. 5(c) and 5(d) and Fig. S6 of the Supplemental Material [34]], consistent with the lack of bound waters seen in the water survival k_{off} analysis [Figs. 3, 4(c), and 4(d)].

III. DISCUSSION

Our results show that biomolecular condensates can be described as networks of interactions that display thermodynamic and kinetic cooperativity, where solubility decreases and molecular exchange slows with growth. Thermodynamically, the solubility is often described by the well-known curvature-controlled exponential, given in Eq. (1) above, which is consistent with the Ostwald-Freundlich or Gibbs-Thomson relation [35,36]. Defining the characteristic radius by $c(r^*) = e^1 c_\infty$ gives us

$$r^* = \frac{2\gamma v}{\phi k_B T}, \tag{2}$$

so r^* grows linearly with interfacial tension γ and protein size v [49]. Our model system shows $r^* \approx 2$ nm, with fitted $\gamma \sim 11$–13 mN m^{-1} with minimal dependence on solubility or lack of interior solvent, yielding a testable thermodynamic criterion that separates *condensates* from *precondensates* for this peptide family.

The characteristic radius coincides with the emergence of a layered core-shell architecture that marks the onset of the condensate regime: a minimum of two peptide layers in the inner core with a corresponding population of bound waters. Bound waters, which have decreased orientational polarizability, should reduce dielectric screening in the interior, strengthening the electrostatic interactions between peptides [50,51]. This influences the value of the stretched exponent in the peptide survival curve in condensate and illustrates the importance of incorporating the effects of explicit water molecules in simulations. It should be noted that coarse-grained models lacking explicit solvent are tuned or fit to give average properties and are not necessarily suited to modeling the varied solvent contributions in different contexts and inhomogeneities [52,53]. Backcalculating nuclear magnetic resonance (NMR) spectra from such models does not capture specific atomic interactions that can contribute to stability of the condensate phase [52].

Kinetically, peptide exchange slows with size according to

$$t_{1/2} \propto r^k, \tag{3}$$

where $k \approx 2.5$, with G (2.3)< S (2.6)< Y (3.4). Pure Lennard-Jones model condensates show $k = 2$ where the survival curve is a simple exponential. Thus, viscoelasticity may play a role in the size of k, with the diffusion constant G (4.8)> S (3.4)> Y (2.4) in units 10^{-12} m^2/s, though more work needs to be done to elucidate factors that modulate k. A simple estimate of the size at which the condensate becomes gel-like, i.e., having a half-life greater than 5 min or 3×10^{11} ns, is G (23 mm)> S (11 mm)> Y (1 mm), at or above the upper limit of condensate sizes *in vivo*. The cooperative effect associated with condensate growth is analogous to the cooperative effect associated with clustering nonpolar (i.e., strongly interacting) amino acids in a protein from a previous study where a protein with nonpolar amino acids clustered together has a half-life in an amyloid fibril orders of magnitude higher than that of an otherwise identical protein with nonpolar amino acids evenly dispersed [54].

The simple exponential model has been the canonical model used to extrapolate protein lifetime in biomolecular condensates, though not without well-known problems, where measurements differ by orders of magnitude across studies [20–22]. Here, a different model is proposed that does not assume each molecule has the same kinetics. Kopelman derived the binding-rate constant for confined fractal-like kinetic systems to be time dependent, $k'_{\text{on}} = k_{\text{on}} t^{\beta-1}$ for $0 < \beta < 1$, where

β is a function of the fractal dimension [23]; here, this was extended to the unbinding rate, with $k'_{\text{off}} = k_{\text{off}} t^{\beta-1}$ for $0 < \beta < 1$:

$$\frac{d[\text{peptide}]_{\text{con}}(t)}{dt} = k_{\text{off}} t^{\beta-1} [\text{peptide}]_{\text{con}}. \tag{4}$$

The solution to the differential equation is then

$$[\text{peptide}]_{\text{con}}(t) = [\text{peptide}]_{\text{con}}(0)\, e^{-(k_{\text{off}}/\beta)t^{\beta}}, \tag{5}$$

where $[\text{peptide}]_{\text{con}}$ is the peptide concentration in the condensate. Results show that k_{off} is sensitive to system size and solubility, while β is not. The stretched exponential has been extensively described in prior literature on glassy liquids and polymers and has recently been theorized in biomolecular condensates as well [55]. The Kohlrausch-Williams-Watts relaxation function as applied to glasses (rough energy landscapes) was termed the trapping model, a generic mathematical model first used to explain the length of time it takes for excitons (molecules, electrons, etc.) to find traps, with the stretching coming from the increased duration the excitons take to find traps once the initial traps have been filled [46]. While earlier papers reporting the value for β have been empirical, the reaction-diffusion equation gives the bifurcation in β to be $d/(d+2)$, where d is a fractal dimension and the effective dimensionality is reduced due to additional constraints [46].

Results found displayed a bifurcation in stretched exponents, with $\beta = 3/5$, i.e., van der Waals-dominated forces ($d = 3$), for the outer shell of the condensate and $\beta = 3/7$, i.e., electrostatic energy-dominated forces ($d = 1.5$), for the inner core. The trapping model assumes the differences in likelihood of exiting a trap are topologically dominated and that the microscopic properties are homogeneous. Thus, qualitative differences in chemical properties within the same condensate may bifurcate their values. Indeed, the electrostatic component of peptide-peptide interactions in the outer shell is expected to be heavily shielded by bulk and surface-associated water, which has a high dielectric constant, while the inner core should be only minimally screened by bound water with a lower dielectric constant [51]. Since there are no interior bound waters in the precondensates, the condensates fit $\beta = 3/5$ very well.

Intuitively, β is an inverse measure of cooperativity, where a lower β means that there is a greater degree of trapping stemming from increased cooperativity, e.g., at the inner core of the condensate due to minimal dielectric screening from water. On the other hand, a higher stretching exponent β would indicate that unbinding rates are more independent of each other. At the extreme case of $\beta = 1$, the unbinding rate is the same for the entire condensate. Indeed, this is seen in water dynamics in condensate, which has two independent unbinding rates for surface and bound waters:

$$[\text{water}]_{\text{con}}(t) = [\text{water}]_{\text{surface}}(0) e^{-k_{\text{off},s}t} + [\text{water}]_{\text{bound}}(0) e^{-k_{\text{off},b}t}, \tag{6}$$

where the off-rates for surface $k_{\text{off},s}$ and bound $k_{\text{off},b}$ water molecules differ by over an order of magnitude (with corresponding half-life of 1 ns versus 10–30 ns, respectively). The bound water half-life is at the low end of experimentally measured internal waters in proteins, which range 6 orders of magnitude from 10 ns to milliseconds [56]. The simple exponential fit for the survival curve of bound water and the independence of water half-life on condensate size suggest that water has readily available exit pathways from individual binding sites (local control), whereas peptide escape reflects collective constraints that grow with size (global or network control). Note that the simple three-site water model used here does not give absolute quantitative agreement for the diffusion constant with experiment and algorithms play a role [57,58], although studies have shown that relative comparisons are informative [59].

The generalizability of our findings to other intrinsically disordered proteins is an important question to address. Our model system uses neutral pentapeptides, which seek to simulate glycine-rich intrinsically disordered proteins with explicit water molecules at a reasonable computational effort. However, intrinsically disordered proteins (IDP) can have $O(10^2)$ amino acids and often contain many charged amino acids. The characteristic radius, or the boundary between condensates and precondensates, increases linearly with molecular volume v and interfacial tension γ based on

the Ostwald-Freundlich equation. For a condensate composed of 100 amino acid with the same interfacial tension as our GGXGG systems, the characteristic radius would be 40 nm, within the realm observable by live-cell super-resolution microscopy. Whether this radius marks the transition of the precondensate to condensate by our definition remains to be explored. Conversely, decreasing the interfacial tension, e.g., with charged amino acids, would decrease the characteristic radius. Moreover, a decrease in the interfacial tension may increase the interfacial width, resulting in more proteins at the outer layer. These predictions may be tested in future computational and/or experimental studies.

IV. CONCLUSIONS

Overall, our findings illustrate emergent properties in liquid-liquid phase separation, where glycine-rich condensates show qualitatively different diffusion-reaction dynamics compared to simpler liquids like water. The results here imply that biomolecular condensates have switchlike thermodynamic cooperative properties and graded kinetic cooperative properties with respect to size. Our study implies that the reaction rate of multiple small condensates would be substantially different from a single large condensate, even if the total number of available proteins between the two systems is the same. This influences how one might understand the role of condensate size in the physiology and pathology of membraneless organelles, e.g., the association between nucleoli size and cancer [11], receptor tyrosine kinase clustering size versus cell fate [8], and differential neurotoxicity between tau oligomers and droplets [15,16]. By extension, this understanding has implications on therapeutic strategies disrupting versus maintaining condensates [57].

V. METHODS

A. Simulation

A total of 21 molecular dynamics simulations were conducted using the namd (Nanoscale Molecular Dynamics) simulation package (version 2.14) to investigate the finite-size effects on liquid-liquid phase separation (LLPS). Three peptide sequences, GGGGG, GGYGG, and GGSGG, known to form aggregates and remain disordered were selected, representing a range of different solubilities. Each peptide sequence was simulated for seven different sizes at the same concentration. Samples of 625, 312, 156, 78, 39, 20, and 10 pentapeptides in water were used (Table S1 of the Supplemental Material [34]). The systems are then referred to as "solute number-center residue" such as 625-G or 39-Y. The box sizes and water content for each simulation were scaled to maintain a constant concentration near 0.3 M across all simulations. The concentration of 0.3 M was selected as it was significantly higher than the solubility limit for these peptides. This was designed so that in an ideal thermodynamic case one might find both a condensed phase and a saturated aqueous phase after equilibration. The high concentration also ensures that most of the peptides are found in the droplet, and so droplet sizes are similar for different peptides of the same sample size, given that they are weakly dependent on solubility. Explicit TIP3P water molecule models were added as used previously [27,60,61]. The simulations were carried out with periodic boundary conditions with the peptide solute placed with Packmol [62], such that they were initially at least 5 Å apart and between 4 and 20 Å from the boundaries, scaled according to box size. This defined the nonequilibrium initial condition for each simulation. The protein force field chosen for this study was CHARMM36m, which has been optimized for IDPs [32]. Note that past publications show a modest dependence of the solubility limit for larger systems ($\sim$625) among standard nonpolarizable force fields [60].

The NPT ensemble (constant number, pressure, and temperature) was used for equilibration [63]. A 2 fs time step was employed. The short-ranged interaction truncation was enabled with a switch turned on at 10 Å and off at 12 Å. The pair list inclusion threshold was set to 14 Å. Rigid bonds were enforced for covalent hydrogen atoms in the system with a tolerance of 10^{-8} Å using the SHAKE algorithm. A Langevin thermostat was used to control the temperature of the system at 300 K, with a damping coefficient of 0.5. Hydrogen atoms were not coupled to the thermostat. A Langevin piston

was used to control the pressure of the system at a target value of 1.01325 bar and a decay time of 100 fs. The piston period was set to 200 fs. The particle-mesh Ewald [64] method was used for long-range electrostatic interactions with a real-space grid spacing of 1.0 Å and a tolerance of 10^{-6} Å.

For diffusion coefficient calculations in the GGGGG simulations, the NVE ensemble (constant number, volume, and energy) was used, with time step reduced to 1 ns, to avoid dynamical artifacts due to the Langevin thermostat [65]. The initial position and velocity for NVE was taken from NPT ensemble runs following a minimum of 300 ns of simulation. The NVE ensembles were simulated for an additional 200 ns.

B. Analysis

1. Aggregate size

The aggregate size for each system was calculated to determine gross structural characteristics of the precondensate/condensate and to aid in determining the excluded volume for the solubility limit analysis. The condensed peptide aggregate phase, in contrast to the aqueous phase, was defined as follows. Two peptides were defined as *clustered* if at least one heavy atom in one peptide was within 4 Å of another. Note that this definition is based on the approximate largest distance between two heavy atoms without the possibility of a water molecule; a sensitivity test showed that the choice of cutoff is relatively insensitive beyond 3.5 Å (Fig. S10 of the Supplemental Material [34]). The largest connected cluster component within the simulation, as defined by graph theory [66], was then identified. All peptides that remained connected to the largest cluster component in a 2-ns window interval were labeled as being a part of the *aggregate*. The aggregate coordinates were defined around its center of geometry. The volume of the aggregate was reconstructed using Delauney triangulation and took an alpha shape of radius 6 Å to determine the coordinates of the condensate surface [67]. The distances of all coordinates from the center of geometry were calculated and took the median (50th percentile), maximum (90th percentile), and minimum (10th percentile) dimensions, giving an approximate estimate of the sphericity. The median of all three of these measures were calculated across at least 200 ns from 2-ns intervals. Finally, the average condensate radius was compared with a function proportional to the cube root of the system size, which is a naïve assumption that condensate volume grows linearly proportional to system size.

2. Solubility limit

To determine the thermodynamic stability of aggregates across different sizes, the solubilities of each system was calculated. Broadly, solubility was calculated by taking the concentration of the peptides in the saturated aqueous phase in the simulation. The overall solubility was quantified by first calculating the total number of free peptides, i.e., peptides not connected to the largest connected component. To use units of molarity, this value was then divided by the effective volume of the solution, determined by subtracting the volume occupied by the identified droplet, as described above in Sec. V B 1, from the simulation volume. Similar techniques have been used previously [27,60]. Calculation for the peptide molecular volume, required to estimate the surface tension in the Ostwald-Freundlich equation, was done using Mol_Volume in VMD [68].

3. Density distribution

The center of geometry for each condensate was determined using the coordinates of all constituent peptides and served as the reference point. To analyze the spatial density of peptides and water within the condensate and beyond, concentric shells were defined around the center of geometry. Data from the first 3 Å from the center of geometry were dropped due to counting noise. Each shell was spaced at 1 Å intervals, and the volume of each shell was calculated accordingly. For each shell, the number of peptides contained within its boundaries was determined. The peptide density within each shell was calculated by dividing the number of peptides in the shell by the

volume of that shell. The obtained values were converted to molar concentration (mol/l). A moving average with a range of 3 Å was used to smooth noise.

Half-life. To gauge the effect of droplet size on the temporal stability of peptides and water molecules, the half-life of the molecules in the condensate across all simulations was calculated. The survival time correlation function $S(t)$ was calculated using

$$S(t) = \frac{1}{N}\sum_{i=1}^{N}\frac{\langle P_i(0)P_i(t)\rangle}{\langle P_i(0)^2\rangle}, \tag{7}$$

where N is the number of peptides or water molecules in condensate; $P_i(t)$ is 1 if it remains in the droplet and $P_i(t)$ is 0 if it leaves the droplet for the ith molecule. A molecule was considered lost for analysis when it departs from the condensate, regardless of whether it rejoins at a later time within the window. What constitutes a peptide belonging to a condensate was defined in Sec. V B 1. For water molecules, all water molecules within a sphere set by the maximum radius of the condensate were defined as belonging to the condensate. The half-life of peptide in an aggregate was defined as the duration $t_{1/2}$ at which $C_{\mathrm{con}}(t_{1/2}) = 0.5$. The half-life of bound water in aggregate was defined as a simple exponential fit from 10 to 50 ns on the survival curve or until it reached one remaining water molecule, whichever came first. The extrapolated half-life from the exponential function was then calculated.

The stretching exponent for peptides was calculated by assuming the survival curve functional form

$$S(t) = e^{-(\frac{t}{\tau_n})^{\beta_n}}, \tag{8}$$

where β_n is the stretching exponent and τ_n is the time-dependent rate constant. β_n was then calculated by taking the linear fit of $\ln[-\ln S] = \beta_n \ln t - \beta_n \ln \tau_n$. The stretching exponent bifurcation (200, 400, and 500 ns for S, G, and Y) was found by examining the stretching exponent at each point versus time (Fig. S4 of the Supplemental Material [34]).

4. Diffusion coefficient

The diffusion coefficient D was calculated for peptides and water molecules in all 21 simulations. The diffusion coefficient was extracted from the mean square displacement (MSD) of the peptide center of geometry using the Einstein relation:

$$\langle (r(t) - r(0))^2\rangle = 6Dt. \tag{9}$$

Only heavy (nonhydrogen) atoms were considered, which, for water, were simply the oxygen atom. For peptides, the time range for which the slope was measured was 20 ps, with 2 ps intervals, while for water, it was 2 ps, with 0.2 ps intervals. Movement due to overall cluster displacement in solution, which can be significant especially for smaller clusters, was subtracted from the MSD (see the Fig. S8 of the Supplemental Material [34] for the effects of translational and rotational correction for 625 GGGGG system). The slopes, measured by the matlab *polyfit* function, were averaged across a 2-ns interval for peptides and a 0.2-ns interval for water. Some evidence of nonlinear anomalous peptide diffusion was observed, especially in the droplet interior, though for the sake of simplicity and because we were only concerned with comparative order of magnitude estimates, linearity between time and MSD was assumed [48]. The distance from the condensate center of geometry was calculated with the coordinates from the first reference frame. To improve sampling statistics for peptide diffusion coefficient, a minimum of 10–2 ns independent intervals were calculated for each simulation.

ACKNOWLEDGMENTS

The authors thank NIH (GM037657) and the Robert A. Welch Foundation (H-0013) for partial support of this work. This work used the Extreme Science and Engineering Discovery Environment

(XSEDE, now ACCESS), which is supported by National Science Foundation Grant No. ACI-1548562. The authors also acknowledge the Texas Advanced Computing Center (TACC) at the University of Texas at Austin for providing HPC resources that have contributed to the research results reported within this paper [69]. The authors thank the scientific computing staff at the Sealy Center for Structural Biology and Molecular Biophysics for computing support.

DATA AVAILABILITY

The data that support the findings of this article are openly available from the authors upon reasonable request. Embargo periods may apply.

[1] V. N. Uversky, Intrinsically disordered proteins in overcrowded milieu: Membrane-less organelles, phase separation, and intrinsic disorder, Curr. Opin. Struct. Biol. **44**, 18 (2017).
[2] D. M. Mitrea and R. W. Kriwacki, Phase separation in biology; functional organization of a higher order, Cell Commun. Signal. **14**, 1 (2016).
[3] C. P. Brangwynne, T. J. Mitchison, and A. A. Hyman, Active liquid-like behavior of nucleoli determines their size and shape in *Xenopus laevis* oocytes, Proc. Natl. Acad. Sci. USA **108**, 4334 (2011).
[4] C. P. Brangwynne, Phase transitions and size scaling of membrane-less organelles, J. Cell Biol. **203**, 875 (2013).
[5] D. S. W. Lee, C. H. Choi, D. W. Sanders, L. Beckers, J. A. Riback, C. P. Brangwynne, and N. S. Wingreen, Size distributions of intracellular condensates reflect competition between coalescence and nucleation, Nat. Phys. **19**, 586 (2023).
[6] N. T. Thanh, N. Maclean, and S. Mahiddine, Mechanisms of nucleation and growth of nanoparticles in solution, Chem. Rev. **114**, 7610 (2014).
[7] P. C. Bressloff, Active suppression of Ostwald ripening: Beyond mean-field theory, Phys. Rev. E **101**, 042804 (2020).
[8] A. Kiyatkin, I. K. van Alderwerelt van Rosenburgh, D. E. Klein, and M. A. Lemmon, Kinetics of receptor tyrosine kinase activation define ERK signaling dynamics, Sci. Signal **13**, eaaz5267 (2020).
[9] J. E. Toettcher, O. D. Weiner, and W. A. Lim, Using optogenetics to interrogate the dynamic control of signal transmission by the Ras/Erk module, Cell **155**, 1422 (2013).
[10] A. Fischer, B. Warscheid, W. Weber, and G. Radziwill, Optogenetic clustering of CNK1 reveals mechanistic insights in RAF and AKT signalling controlling cell fate decisions, Sci. Rep. **6**, 38155 (2016).
[11] M. S. Heltberg, A. Lucchetti, F. S. Hsieh, D. P. Minh Nguyen, S. H. Chen, and M. H. Jensen, Enhanced DNA repair through droplet formation and p53 oscillations, Cell **185**, 4394 (2022).
[12] M. Derenzini, D. Trerè, A. Pession, L. Montanaro, V. Sirri, and R. L. Ochs, Nucleolar function and size in cancer cells, Am. J. Pathol. **152**, 1291 (1998).
[13] V. Tiku, C. Jain, Y. Raz, S. Nakamura, B. Heestand, W. Liu, M. Spath, H. E. D. Suchiman, R. U. Muller, P. E. Slagboom, *et al.*, Small nucleoli are a cellular hallmark of longevity, Nat. Commun. **8**, 16083 (2017).
[14] X. Gui, S. Feng, Z. Li, Y. Li, B. Reif, B. Shi, and Z. Niu, Liquid-liquid phase separation of amyloid-beta oligomers modulates amyloid fibrils formation, J. Biol. Chem. **299**, 102926 (2023).
[15] S. S. Shafiei, M. J. Guerrero-Munoz, and D. L. Castillo-Carranza, Tau oligomers: Cytotoxicity, propagation, and mitochondrial damage, Front. Aging Neurosci. **9**, 83 (2017).
[16] N. M. Kanaan, C. Hamel, T. Grabinski, and B. Combs, Liquid-liquid phase separation induces pathogenic tau conformations *in vitro*, Nat. Commun. **11**, 2809 (2020).
[17] C. M. Cowan and A. Mudher, Are tau aggregates toxic or protective in tauopathies? Front. Neurol. **4**, 114 (2013).
[18] P. G. Vekilov, Dense liquid precursor for the nucleation of ordered solid phases from solution, Cryst. Growth Des. **4**, 671 (2004).

[19] J. D. Forman-Kay, J. A. Ditlev, M. L. Nosella, and H. O. Lee, What are the distinguishing features and size requirements of biomolecular condensates and their implications for RNA-containing condensates? RNA **28**, 36 (2022).
[20] N. O. Taylor, M. T. Wei, H. A. Stone, and C. P. Brangwynne, Quantifying dynamics in phase-separated condensates using fluorescence recovery after photobleaching, Biophys. J. **117**, 1285 (2019).
[21] M. L. Heltberg, J. Mine-Hattab, A. Taddei, A. M. Walczak, and T. Mora, Physical observables to determine the nature of membrane-less cellular sub-compartments, eLife **10**, e69181 (2021).
[22] D. T. McSwiggen, M. Mir, X. Darzacq, and R. Tjian, Evaluating phase separation in live cells: Diagnosis, caveats, and functional consequences, Genes Dev. **33**, 1619 (2019).
[23] R. Kopelman, Fractal reaction kinetics, Science **241**, 1620 (1988).
[24] T. Mittag and R. V. Pappu, A conceptual framework for understanding phase separation and addressing open questions and challenges, Mol. Cell **82**, 2201 (2022).
[25] M. Abbas, W. P. Lipiński, K. K. Nakashima, W. T. S. Huck, and E. Spruijt, A short peptide synthon for liquid–liquid phase separation, Nat. Chem. **13**, 1046 (2021).
[26] M. Auton, D. W. Bolen, and J. Rösgen, Structural thermodynamics of protein preferential solvation: Osmolyte solvation of proteins, aminoacids, and peptides, Proteins **73**, 802 (2008).
[27] D. Karandur, K. Y. Wong, and B. M. Pettitt, Solubility and aggregation of Gly_5 in water, J. Phys. Chem. B **118**, 9565 (2014).
[28] D. Asthagiri, D. Karandur, D. S. Tomar, and B. M. Pettitt, Intramolecular interactions overcome hydration to drive the collapse transition of Gly_{15}, J. Phys. Chem. B **121**, 8078 (2017).
[29] J. A. Drake and B. M. Pettitt, Thermodynamics of conformational transitions in a disordered protein backbone model, Biophys. J. **114**, 2799 (2018).
[30] A. I. Hentati and L. C. Fourati, Comprehensive survey of UAVs communication networks, Compu. Stand. Interfaces **72**, 103451 (2020).
[31] A. Sheng, Q. Su, L. Wang, and J. B. Plotkin, Strategy evolution on higher-order networks, Nat. Comput. Sci. **4**, 274 (2024).
[32] J. Huang, S. Rauscher, G. Nawrocki, T. Ran, M. Feig, B. L. de Groot, H. Grubmüller, and A. D. MacKerell, CHARMM36m: An improved force field for folded and intrinsically disordered proteins, Nat. Methods **14**, 71 (2017).
[33] Laicheng Zhou, L. Z., Cong Wang, Tengyan Xu, Jing Wang, Bin Zhang, Xin Zhang, and Huaimin Wang, Multiphasic condensates formed with monocomponent of tetrapeptides via phase separation, Nat. Commun. **16**, 2706 (2025).
[34] See Supplemental Material at http://link.aps.org/supplemental/10.1103/kbfb-d5nk for simulation concentration specifications for each system, solubility fluctuations in time, solubility versus radis plots and density distributions for the systems. Survival time parameter estimates and the spatial dependence of simple diffusion coefficients are given.
[35] M. Perez, Gibbs–Thomson effects in phase transformations, Scr. Mater. **52**, 709 (2005).
[36] A. K. Shchekin and A. I. Rusanov, Generalization of the Gibbs–Kelvin–Köhler and Ostwald–Freundlich equations for a liquid film on a soluble nanoparticle, J. Chem. Phys. **129**, 154116 (2008).
[37] M. Kidokoro, The interfacial tensions between hexane and aqueous salt solutions, Bull. Chem. Soc. Jpn. **7**, 280 (1932).
[38] Z. Benayad, S. von Bülow, L. S. Stelzl, and G. Hummer, Simulation of FUS protein condensates with an adapted coarse-grained model, J. Chem. Theory Comput. **17**, 525 (2021).
[39] G. L. Dignon, W. Zheng, R. B. Best, Y. C. Kim, and J. Mittal, Relation between single-molecule properties and phase behavior of intrinsically disordered proteins, Proc. Natl. Acad. Sci. USA **115**, 9929 (2018).
[40] A. Nomoto, S. Nishinami, and K. Shiraki, Solubility parameters of amino acids on liquid-liquid phase separation and aggregation of proteins, Front. Cell Dev. Biol. **9**, 691052 (2021).
[41] J. P. Hansen and I. R. McDonald, *Theory of Simple Liquids* (Academic Press, Oxford, 1976).
[42] D. Karandur, R. C. Harris, and B. M. Pettitt, Protein collapse driven against solvation free energy without H-bonds, Protein Sci. **25**, 103 (2016).
[43] G. Reddy, J. E. Straub, and D. Thirumalai, Dynamics of locking of peptides onto growing amyloid fibrils, Proc. Natl. Acad. Sci. USA **106**, 11948 (2009).

[44] J. P. Brady, P. J. Farber, A. Sekhar, Y. H. Lin, R. Huang, A. Bah, T. J. Nott, H. S. Chan, A. J. Baldwin, J. D. Forman-Kay, *et al.*, Structural and hydrodynamic properties of an intrinsically disordered region of a germ cell-specific protein on phase separation, Proc. Natl. Acad. Sci. USA **114**, E8194 (2017).

[45] A. C. Murthy, G. L. Dignon, Y. Kan, G. H. Zerze, S. H. Parekh, J. Mittal, and N. L. Fawzi, Molecular interactions underlying liquid−liquid phase separation of the FUS low-complexity domain, Nat. Struct. Mol. Biol. **26**, 637 (2019).

[46] J. C. Phillips, Stretched exponential relaxation in molecular and electronic glasses, Rep. Prog. Phys. **59**, 1133 (1996).

[47] C. Huang and B. M. Pettitt, Parameter dependence of the solubility limit for disodium phosphate, J. Phys. Chem. B **127**, 8690 (2023).

[48] R. J. Workman, C. J. Huang, G. C. Lynch, and B. M. Pettitt, Peptide diffusion in biomolecular condensates, Biophys. J. **123**, 1668 (2024).

[49] M. Iwamatsu, Nucleation and growth by diffusion under Ostwald-Freundlich boundary condition, J. Chem. Phys. **140**, 064702 (2014).

[50] T. Dufils, C. Schran, J. Chen, A. K. Geim, L. Fumagalli, and A. Michaelides, Origin of dielectric polarization suppression in confined water from first principles, Chem. Sci. **15**, 516 (2024).

[51] R. J. Workman, A. E., G. C. Lynch, C. J. Huang, A. D. MacKerell, Jr., and B. M. Pettitt, Polarizability determines structure of biomolecular condensates, Biophys. J. (to be published).

[52] A. P. Lyubartsev, Inverse Monte Carlo methods, in *Coarse Grained Modeling of Biomolecules*, edited by G. A. Papoian (CRC Press, Boca Raton, FL, 2018), pp. 1–26.

[53] A. Emelianova , P. L. Garcia, D. Tan , and J. A. Joseph , Prediction of small-molecule partitioning into biomolecular condensates from simulation, JACS Au **5**, 3125 (2025).

[54] C. Huang, E. Ghanati, and J. D. Schmit, Theory of sequence effects in amyloid aggregation, J. Phys. Chem. B **122**, 5567 (2018).

[55] R. Takaki, L. Jawerth, M. Popović, and F. Jülicher, Theory of rheology and aging of protein condensates, PRX Life **1**, 13 (2023).

[56] M. Tarek and D. J. Tobias, The dynamics of protein hydration water: A quantitative comparison of molecular dynamics simulations and neutron-scattering experiments, Biophys. J. **79**, 3244 (2000).

[57] S. von Bülow, J. T. Bullerjahn, and G. Hummer, Systematic errors in diffusion coefficients from long-time molecular dynamics simulations at constant pressure, J. Chem. Phys. **153**, 021101 (2020).

[58] S. Najafi, S. Lobo, M. S. Shell, and J.-E. Shea, Context dependency of hydrophobicity in intrinsically disordered proteins: Insights from a new dewetting free energy-based hydrophobicity scale, J. Phys. Chem. B **129**, 1904 (2025).

[59] M. C. Bellissent-Funel, A. Hassanali, M. Havenith, R. Henchman, P. Pohl, F. Sterpone, D. van der Spoel, Y. Xu, and A. E. Garcia, Water determines the structure and dynamics of proteins, Chem. Rev. **116**, 7673 (2016).

[60] R. Sarma, K. Y. Wong, G. C. Lynch, and B. M. Pettitt, Peptide solubility limits: Backbone and side-chain interactions, J. Phys. Chem. B **122**, 3528 (2018).

[61] R. J. Workman and B. M. Pettitt, Thermodynamic compensation in peptides following liquid-liquid phase separation, J. Phys. Chem. B **125**, 6431 (2021).

[62] L. Martinez, R. Andrade, E. G. Birgin, and J. M. Martinez, PACKMOL: A package for building initial configurations for molecular dynamics simulations, J. Comput. Chem. **30**, 2157 (2009).

[63] J. C. Phillips, D. J. Hardy, J. D. C. Maia, J. E. Stone, J. V. Ribeiro, R. C. Bernardi, R. Buch, G. Fiorin, J. Henin, W. Jiang, *et al.*, Scalable molecular dynamics on CPU and GPU architectures with NAMD, J. Chem. Phys. **153**, 044130 (2020).

[64] T. Darden, D. York, and L. Pedersen, Particle mesh Ewald: An $N\cdot(N)$ method for Ewald sums in large systems, J. Chem. Phys. **98**, 10089 (1993).

[65] J. T. Bullerjahn, S. von Bulow, M. Heidari, J. Henin, and G. Hummer, Unwrapping NPT simulations to calculate diffusion coefficients, J. Chem. Theory Comput. **19**, 3406 (2023).

[66] J. Clark and D. A. Holton, *A First Look at Graph Theory* (World Scientific, Singapore, 1991).

[67] W. Zhou and H. Yan, Alpha shape and Delaunay triangulation in studies of protein-related interactions, Briefings Bioinf. **15**, 54 (2014).
[68] A. Balaeff, Mol_Volume: A program for calculating the macromolecular volume (University of Illinois, 2001), https://www.ks.uiuc.edu/Development/MDTools/molvolume/.
[69] Texas Advanced Computing Center, http://www.tacc.utexas.edu/.